

RESEARCH ARTICLE | NOVEMBER 01 2024

# Metamaterial unipolar quantum optoelectronics for mid-infrared free-space optics

Special Collection: [Mid-IR Photonics](#), [2024 Future Luminary Collection](#)T. Bonazzi; H. Dely ; P. Didier ; D. Gacemi ; B. Fix ; M. Beck ; J. Faist ; A. Harouri ; I. Sagnes ; F. Grillot ; A. Vasanelli ; C. Sirtori  

APL Photonics 9, 110801 (2024)

<https://doi.org/10.1063/5.0225920>

## Articles You May Be Interested In

Progress in mid-infrared optoelectronics for high-speed free-space data throughput


APL Photonics (January 2025)

Performance analysis of 4800bps FSK acoustic modem for short range underwater communication

AIP Conf. Proc. (February 2023)


A pilot investigation on real time multi-view high efficiency video coding

AIP Conf. Proc. (December 2023)



**Your One-Stop Shop for the Best Brands in Optics**

- Extensive inventory with over 34,000 products available & 2,900 new products
- Fast shipping from our 9 distribution centres around the globe
- Bringing 80+ years of optical expertise to customers worldwide

 **Edmund**  
optics | worldwide

[Shop Now](#)

# Metamaterial unipolar quantum optoelectronics for mid-infrared free-space optics

Cite as: APL Photon. 9, 110801 (2024); doi: 10.1063/5.0225920

Submitted: 27 June 2024 • Accepted: 14 October 2024 •

Published Online: 1 November 2024



T. Bonazzi,<sup>1</sup> H. Dely,<sup>1</sup>  P. Didier,<sup>2</sup>  D. Gacemi,<sup>1</sup>  B. Fix,<sup>3</sup>  M. Beck,<sup>4</sup>  J. Faist,<sup>4</sup>  A. Harouri,<sup>5</sup>   
I. Sagnes,<sup>5</sup>  F. Grillot,<sup>2</sup>  A. Vasanelli,<sup>1,a)</sup>  and C. Sirtori<sup>1,b)</sup> 

## AFFILIATIONS

<sup>1</sup>Laboratoire de Physique de l'ENS, Département de Physique, École Normale Supérieure, Université PSL, Sorbonne Université, Université Paris Cité, CNRS, 75005 Paris, France

<sup>2</sup>Télécom Paris, Institut Polytechnique de Paris, LTCI, Palaiseau, France

<sup>3</sup>DOTA, ONERA, Université Paris-Saclay, F-91123 Palaiseau, France

<sup>4</sup>Institute for Quantum Electronics, ETH Zürich, CH-8093 Zürich, Switzerland

<sup>5</sup>Université Paris-Saclay, CNRS, Centre de Nanosciences et de Nanotechnologies, Palaiseau 91120, France

**Note:** This paper is part of the APL Photonics Special Topic on Mid-IR Photonics.

<sup>a)</sup>Electronic mail: [angela.vasanelli@ens.fr](mailto:angela.vasanelli@ens.fr)

<sup>b)</sup>Author to whom correspondence should be addressed: [carlo.sirtori@ens.fr](mailto:carlo.sirtori@ens.fr)

## ABSTRACT

Free-space optical communications in the mid-infrared transparency windows (4–5 and 8–14  $\mu\text{m}$  wavelength regions) is emerging as a viable solution for high bitrate data transmission. Unipolar quantum optoelectronics is the technology of choice for data communication in this wavelength region, thanks to the high frequency response of detectors and modulators. In this work, it is demonstrated that the performances of these devices can be substantially enhanced by embedding them into metamaterials. It is also shown that metamaterials have to be engineered differently in detectors than in modulators, as the role of light–matter interaction must be tuned adequately in the two devices. Metamaterial-enhanced performances allow the realization of data transmission with a record rate of 68 Gbit/s, while ensuring robustness and consistency, as it should be for real-world applications. These findings underscore the promising role of metamaterial-enhanced unipolar devices in advancing free-space optical communication systems.

© 2024 Author(s). All article content, except where otherwise noted, is licensed under a Creative Commons Attribution (CC BY) license (<https://creativecommons.org/licenses/by/4.0/>). <https://doi.org/10.1063/5.0225920>

## I. INTRODUCTION

Global data transmission is witnessing an unprecedented surge in daily data flows and keeps on increasing the need for dependable high-speed data communication. Free-Space Optics (FSO) has attracted interest as a possible solution to the so-called “last mile” connectivity problems,<sup>1</sup> to replace fiber connections whenever their installation is too expensive or not permanent. Remarkable achievements have been made in data rate transmission, reaching the terabits per second, particularly in the telecom wavelength range at  $\approx 1.5 \mu\text{m}$ .<sup>2</sup> However, the mid-infrared (MIR) wavelength domain, specifically within 8–14  $\mu\text{m}$ , holds promise for FSO applications. This is primarily due to its atmospheric transparency, reduced light-scattering to micrometric aerosols, and resilience in adverse

atmospheric conditions, including turbulence.<sup>3–5</sup> Several light sources are available in this wavelength range, including optical parametric oscillators,<sup>6,7</sup> supercontinuum generation sources,<sup>8,9</sup> and quantum cascade lasers<sup>10</sup> (QCLs). QCLs have proven their utility across diverse applications such as spectroscopy,<sup>11,12</sup> medicine,<sup>13,14</sup> and FSO telecommunications.<sup>15–18</sup> Notably, some FSO telecommunications have achieved impressive results by employing frequency conversion from 1.5 to 3.4  $\mu\text{m}$  wavelengths, resulting in data rates reaching hundreds of Gbit/s.<sup>19</sup> Nevertheless, these achievements still face challenges related to low MIR output power and high power consumption associated with near-infrared pump lasers.

Unipolar quantum devices rely on optical transitions between electronic states in the conduction band of semiconductor quantum wells. Therefore, they have some physical properties that make them

suitable for mid-infrared FSO, namely, the very short lifetime of the electrons in the excited states and the wavelength agility within the atmospheric transparency windows. Wavelength agility, which is the possibility of choosing the device photon energy, is not related to intrinsic material properties, such as the energy gap, but rather to the design of the semiconductor heterostructure, in which the thicknesses of the layers are controlled with Å precision by epitaxial growth. The extremely short excited state lifetime in semiconductor quantum wells, in the order of 1 ps,<sup>20</sup> leads to unipolar devices with electrical bandwidths that exceed 100 GHz.<sup>21</sup> Moreover, such a short lifetime results in unipolar detectors<sup>22</sup> with a high saturation power, ideal for coherent heterodyne detection.<sup>23</sup> Detectors,<sup>24</sup> modulators,<sup>25</sup> and laser sources<sup>26</sup> operating in this scientific context form a versatile platform of devices in the mid-infrared spectral range, known under the name of Unipolar Quantum Optoelectronics (UQO).

Recently, free-space data transmission in the mid-infrared has been demonstrated using a system entirely based on UQO devices.<sup>25</sup> The system, composed of a quantum cascade laser, a quantum cascade detector,<sup>27</sup> and an external Stark modulator,<sup>28</sup> demonstrated 10 Gbit/s free-space data transmission at 9  $\mu\text{m}$ . A second demonstration, involving pulse shaping and pre- and post-processing, showed data transmission at 30 Gbit/s over a 31-m link with the same carrier wavelength.<sup>29</sup> In these two demonstrations, the detector and the modulator were fabricated in mesa architectures and with high-frequency packaging by connecting the mesa to a coplanar waveguide through an air-bridge.<sup>22</sup> In these devices, light coupling was ensured by a 45° polished facet to comply with the polarization selection rule, stating that intraband optical transitions occur only when light is polarized along the quantum well growth direction. This architecture is very advantageous for the realization of high-speed unipolar devices but a net increase in the performances is obtained when it is associated with photonic structures.

Indeed, embedding the heterostructure of UQO devices within metamaterials allows the engineering of an ad hoc electromagnetic environment. Several examples can be found in the literature on metamaterial-based quantum cascade lasers,<sup>30–32</sup> unipolar detectors,<sup>33–39</sup> amplitude,<sup>40,41</sup> and phase<sup>42</sup> modulators.

The specific photonic metamaterial used for our devices enhances the light-matter coupling strength, reduces the electrical area, and works for normal incidence optical beams. The light-matter interaction is enhanced as photons have a longer lifetime in metamaterial resonators. However, the coupling of the free space radiation with the material has to be engineered differently, depending on the device function within the system. Indeed, the light-matter interaction is not tailored for modulators as it is for detectors, as we describe in Sec. II by using coupled mode theory. Metamaterials also allow a net separation between the optical and the electrical area, thanks to the antenna effect that gathers light on a collection area much larger than the antenna size. This is exploited to minimize the device electrical area, thus its geometrical capacitance, to optimize high frequency operation, as described in Sec. III. Finally, antennae enable UQO devices to operate at normal incidence, yet satisfying the polarization selection rule. All these improvements are very beneficial for the implementation of high-speed mid-infrared systems for applications. In this work, we focus on the realization of FSO data transmission systems designed to take full advantage of metamaterial UQO devices.

## II. METAMATERIAL UNIPOLAR DEVICES

Our devices consist of a one-dimensional array of metal-semiconductor-metal (MIM) stripe resonators, of period  $p$ , as illustrated in Fig. 1(a). Each stripe, of width  $s$  and thickness  $H$ , contains an ensemble of doped quantum wells, playing the role of the device's active region. Each stripe behaves as a Fabry-Perot resonator, such that the stripe width is related to the cavity resonance  $\omega_{\text{cav}}$  through  $\omega_{\text{cav}} = \pi c / (n_{\text{eff}} s)$ , with  $n_{\text{eff}}$  the effective index of the cavity mode.<sup>43</sup> The stripe thickness and the array period determine the coupling with free-space radiation. To ensure high-frequency operation for data transmission, the  $50 \times 50 \mu\text{m}^2$  array is coupled to a coplanar waveguide through an air bridge, as can be seen in the scanning electron microscope image of one of our devices presented in Fig. 1(c).

The coupling between the resonator mode, embedding the device active region, and the free-space radiation can be well

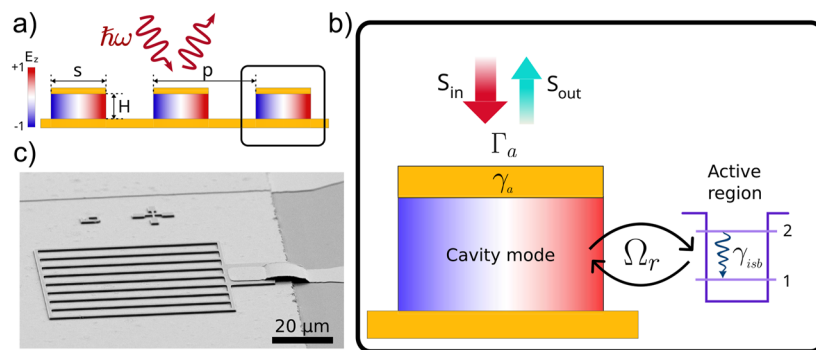


**FIG. 1.** Metamaterial unipolar quantum devices. (a) Sketch of an array of stripes with its main geometrical parameters: the stripe width  $s$ , spacing  $p$ , and height  $H$ . The component along the growth direction of the electric field confined within the stripes at the resonance frequency is plotted in a normalized color scale. (b) Coupled mode theory representation of the system. The incoming field  $S_{\text{in}}$  couples to the cavity electromagnetic mode, which is coupled to the active region polarization mode. The amplitude of the reflected field is denoted  $S_{\text{out}}$ . (c) Scanning electron microscope image of a device. The active material is embedded within gold stripes and a bottom metallic layer. The stripes are connected through an air bridge to a coplanar waveguide for radio frequency injection.

described by temporal coupled mode theory, in which a single mode resonator can couple with multiple ports.<sup>44</sup> This approach has already been used to engineer photon absorption in unipolar quantum devices.<sup>45</sup> In Sec. II A, we will discuss the coupled mode theory applied to the design of metamaterial-based quantum cascade detectors and Stark modulators.

### A. Coupled mode theory for MIM resonator arrays coupled with an intraband polarization in a quantum well

Conceptually, the metamaterial device is composed of two coupled oscillators. The first oscillator is the cavity TM<sub>01</sub>-mode, at frequency  $\omega_{cav}$ . The second oscillator is the intersubband (intra-band) polarization associated with the optical transition between the ground and the first excited state of the quantum well. The intraband polarization oscillates at frequency  $\tilde{\omega}_{ISB}$ , which is shifted from the frequency separation between the two electronic states,  $\omega_{ISB}$ , following:  $\tilde{\omega}_{ISB}^2 = \omega_{ISB}^2 + \omega_P^2$ . Here,  $\omega_P$  is the plasma frequency associated with the transition, expressed as  $\omega_P = \sqrt{n_s e^2 f_{ISB} / (m^* \epsilon_r \epsilon_0 L_{eff})}$ , with  $n_s$  the areal electronic density in the wells,  $f_{ISB}$  the oscillator strength of the transition,  $m^*$  the electron effective mass,  $\epsilon_0 \epsilon_r$  the permittivity of the medium, and  $L_{eff}$  the intraband transition effective length.<sup>46</sup>

The coupling between the cavity mode and the intraband polarization induces new eigenfrequencies following the dispersion relation<sup>47</sup>

$$(\omega^2 - \tilde{\omega}_{ISB}^2)(\omega^2 - \omega_{cav}^2) = 4\Omega_R^2 \omega_{cav}^2, \quad (1)$$

where the Rabi frequency  $\Omega_R$  is directly related to the plasma frequency through  $2\Omega_R = \sqrt{f_w \omega_P}$ ,  $f_w$  being the spatial overlap factor between the cavity mode and the intraband polarization in the quantum well. From Eq. (1), it is easy to understand that the value of  $\Omega_R$  is the coupling strength between the oscillators. Several light-matter coupling regimes, controlled by the magnitude of  $\Omega_R$ , can be differentiated by observing the absorption spectra, especially when  $\omega_{cav} = \tilde{\omega}_{ISB}$ , where the frequency separation between the two branches reaches a minimum value of  $2\Omega_R$ . In the weak coupling regime, the separation cannot be observed due to energy losses exceeding the splitting energy, and only a single enhanced peak around  $\omega_{cav}$  exists. The cavity and the polarization absorb cooperatively the incident radiation, which may result in a critical coupling when the total losses match the electromagnetic field injection rate. When the coupling frequency is increased, the absorption peak will split in two, revealing two polaritonic excitations, separated by  $2\Omega_R$ , characteristic of the strong coupling regime. In the event of very high values of  $\Omega_R$ , the two asymptotic frequencies of the polaritons

exhibit a significant gap in the order of  $2\Omega_R^2/\omega_{ISB}$  and the system enters the so-called ultrastrong coupling regime.<sup>48</sup> All these regimes can be used to engineer the best operation of unipolar metamaterial devices as we will explain in the following sections for QCDs and Stark-based modulators.

The coupled-mode theory describes the optical properties of the devices in the weak and strong coupling regimes.<sup>45</sup> The incident radiation with power  $|S_{in}|^2$  excites the electric field of the cavity mode (of amplitude  $a$ ) at a rate of  $\Gamma_a$ . This radiative loss coefficient  $\Gamma_a$  depends on the periodicity  $p$  and the height  $H$  through  $\Gamma_a = C \frac{H}{p^2}$ , where  $C$  is a constant.<sup>45</sup> The non-radiative dissipation channel of the cavity is introduced through a damping term  $\gamma_a$ , accounting for the Joule losses in the metal, in the doped semiconductor contacts, and also scattering from the device surfaces. The polarization field  $P$  associated with the intraband transition is coupled with the cavity mode with a rate of  $\Omega_R$ . It is also characterized by a non-radiative damping rate  $\gamma_{ISB}$ , due to scattering with phonons, alloy disorder, and interface roughness. The typical timescale of these processes is  $<1$  ps, which is much shorter than the typical radiative spontaneous emission time of the optical transition, 100 ns. This observation explains why radiative re-emission can be neglected. The power of the outgoing radiation is indicated as  $|S_{out}|^2$ . Figure 1(b) schematizes the resonator coupled with the intraband polarization and indicates the different quantities introduced in the coupled mode description of the system.

With the previously introduced notation, the temporal evolution of the cavity field and intraband polarization reads

$$\begin{cases} \partial_t a = -(\gamma_a + \Gamma_a)a + i\omega_{cav}a + i\Omega_R P + \sqrt{2\Gamma_a}S_{in} \\ \partial_t P = -\gamma_{ISB}P + i\tilde{\omega}_{ISB}P + i\Omega_R a \\ S_{out} = -S_{in} + \sqrt{2\Gamma_a}a \end{cases}. \quad (2)$$

Considering a monochromatic incident radiation,  $S_{in} = s_0 e^{i\omega t}$ , the system of Eq. (2) facilitates the computation of key parameters for our investigation, which are the cavity absorptivity  $A_{cav}$ , the intraband absorptivity  $A_{ISB}$ , and the total absorptivity  $A_{tot}$ , defined as

$$\begin{cases} A_{cav} = 2\gamma_a \frac{|a|^2}{|S_{in}|^2} \\ A_{ISB} = 2\gamma_{ISB} \frac{|P|^2}{|S_{in}|^2} \\ A_{tot} = A_{cav} + A_{ISB} \end{cases}. \quad (3)$$

From Eqs. (2) and (3), the expression of the total energy dissipated in the system turns out to be

$$A_{tot}(\omega) = \frac{4\Gamma_a(\gamma_a(\gamma_{ISB}^2 + (\omega - \tilde{\omega}_{ISB})^2) + \gamma_{ISB}\Omega_R^2)}{((\gamma_a + \Gamma_a)(\omega - \tilde{\omega}_{ISB}) + \gamma_{ISB}(\omega - \omega_{cav}))^2 + ((\gamma_a + \Gamma_a)\gamma_{ISB} - (\omega - \tilde{\omega}_{ISB})(\omega - \omega_{cav}) + \Omega_R^2)^2}. \quad (4)$$

The reflectivity spectrum of the device is obtained from  $A_{tot}$  in a straightforward manner, as briefly recalled in Appendix A. Please note that Eq. (2) fails in describing the ultrastrong coupling regime

as they do not account for the antiresonant terms involving  $a^*$  and  $P^*$ , which are fundamental to correctly describing the specific features of this regime, such as the widening of the polaritonic gap.

## B. Metamaterial quantum cascade detector

Our detector is a quantum cascade detector (QCD) based on a diagonal design.<sup>49</sup> QCDs are unipolar infrared photodetectors<sup>27</sup> that can operate in photovoltaic mode up to room temperature. The active region is based on the periodic repetition of tunnel-coupled quantum wells. Figure 2(a) represents one period of the QCD: mid-infrared photons are absorbed through an intraband transition between two confined states. Photoexcited electrons relax, mainly by scattering with longitudinal optical phonons, toward the ground state of the following period of the cascade. The QCD operates in photovoltaic mode due to the asymmetry of the cascade region that acts as a pseudo-electric field, driving the electrons in one direction only, thus giving rise to a photocurrent.

The QCD was first characterized in mesa geometry. Figure 2(b) presents the photocurrent spectrum measured at 78 K in photovoltaic mode. Two peaks are observed, associated with the intraband transitions 1 → 2 (at a wavelength of 10 μm) and 1 → 3. We optimized the device photoresponse at 10 μm using the metamaterial resonator presented above. In this diagonal design of the active region, the oscillator strength of the 1–2 transition is  $f_{12} = 0.41$ . Considering the electronic density of  $10^{18} \text{ cm}^{-3}$ , the Rabi energy is calculated to be  $\hbar\Omega_R = 6.9 \text{ meV}$  and the metamaterial QCD operates in the light–matter weak coupling regime. The width of

the stripe sustaining a mode resonant with the intraband transition  $E_{12} = E_2 - E_1$  is calculated to be  $s = 1.4 \text{ μm}$ . The quantity to be optimized for the metamaterial design is the QCD responsivity, given by  $R = \frac{e\lambda}{hc} \times g A_{ISB}$ , where  $g$  is the photoconductive gain and  $A_{ISB}$  is the absorption efficiency. The photoconductive gain is inversely proportional to the number of periods in the cascade. It can thus be optimized by reducing the structure thickness. However, this reduction comes at the expense of the device's capacitance and consequently of the frequency bandwidth. We decided to set to 9 the number of periods of the cascade for a total height without contacts of 416 nm. The array periodicity, which sets the radiative losses once the thickness of the cavity has been fixed, has to be chosen to maximize the absorption efficiency. From the coupled mode theory presented before,  $A_{ISB}$  in the weak coupling regime and at resonance is given by

$$A_{ISB}(\omega = \omega_{cav} = \tilde{\omega}_{ISB}) = \frac{4\gamma_{ISB}\Gamma_a\Omega_R^2}{(\gamma_{ISB}(\gamma_a + \Gamma_a) + \Omega_R^2)^2}. \quad (5)$$

By imposing that the absorption efficiency is maximum with respect to a variation of the radiative cavity losses, we obtain:

$$\frac{\partial A_{ISB}}{\partial \Gamma_a} = 0 \Leftrightarrow \Gamma_a = \frac{\Omega_R^2}{\gamma_{ISB}} + \gamma_a. \quad (6)$$

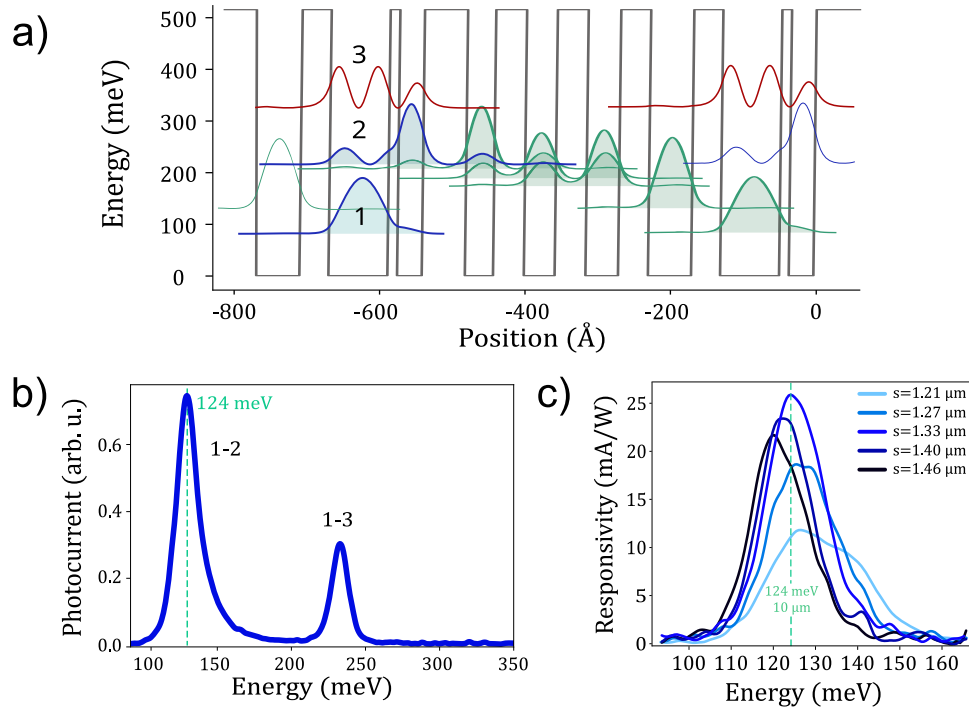


**FIG. 2.** Quantum cascade detector in a metamaterial architecture. (a) Simulated conduction band diagram of one period and a half of our GaInAs/AlInAs quantum cascade detector. The square moduli of the relevant wavefunctions are plotted at the corresponding energies. The thicknesses (in nm) of the layers (InGaAs wells are in bold) composing one period of the structure are 6.7, 1.1, 2.8, 4.9, 3.2, 3.5, 3.5, 3.5, 3.7, 3.4, 4.9, 3.3. The first quantum well is doped with a density of  $n_{3D} = 10^{18} \text{ cm}^{-3}$ . The total structure contains 9 periods. (b) Photocurrent spectrum measured at 78 K and zero bias on a mesa device. The two observed resonances correspond to the 1–2 (at 124 meV) and 1–3 (240 meV) electronic transitions. (c) Responsivity spectra measured at room temperature and zero bias on metamaterial devices with different values of the stripe width  $s$ .

**TABLE I.** CMT parameters for Stark modulator and QCD extracted from the reflectivity spectra of arrays of metamaterials with various values of  $p$  (3, 4, 5, 6, 7  $\mu\text{m}$ ) and  $s$  (six values between 1.2 and 1.8  $\mu\text{m}$ ).

Modulator					QCD				
$\hbar\Gamma_a \times p^2$ meV $\mu\text{m}^2$	$\hbar\gamma_a$ meV	$\hbar\gamma_{ISB}$ meV	$\hbar\Omega_R$ meV	$n_{eff}$	$\hbar\Gamma_a \times p^2$ meV $\mu\text{m}^2$	$\hbar\gamma_a$ meV	$\hbar\gamma_{ISB}$ meV	$\hbar\Omega_R$ meV	$n_{eff}$
151	2.3	20.1	13.6	3.65	87	2.5	16.9	6.9	3.65

This corresponds to the critical coupling condition: the cavity radiative losses must balance all the other losses in the system for maximum absorption. The choice of  $p$  satisfying the critical coupling condition necessitates an accurate knowledge of all the losses in the system. To this aim, we followed the approach presented in Ref. 45. A first set of devices with different stripe dimensions (between 1.3 and 1.7  $\mu\text{m}$ ) and periodicity (between 3 and 6  $\mu\text{m}$ ) were fabricated following the procedure presented in Appendix B. These devices were characterized by performing reflectivity experiments in a set-up with a Cassegrain microscope objective coupled to a Fourier Transform Infrared Spectrometer and a commercial Mercury Cadmium Telluride detector. The fitting of the measured spectra using the reflectivity expression given by the coupled mode theory allowed us to extract the relevant parameters for the coupled mode theory model, which are summarized in Table I. Using these parameters, we were able to set the optimum periodicity for the metamaterial QCD to  $p = 4 \mu\text{m}$ . Figure 2(c) presents the responsivity spectra of five metamaterial QCDs with various widths, ranging from 1.21 to 1.46  $\mu\text{m}$ , and fixed period. The maximum responsivity is achieved for  $s = 1.33 \mu\text{m}$ . This does not correspond exactly to the resonance condition extracted from reflectivity experiments since the extraction probability (entering the expression of the photoconductive gain) depends on the spectral shape of the extractor.<sup>50</sup> The responsivity spectra were calibrated from the measure of the responsivity of the device with  $s = 1.33 \mu\text{m}$  under illumination by a quantum cascade laser emitting 50 mW at 123 meV. This

responsivity, reaching 26 mA/W at 124 meV for this device, is ten times larger than that measured on a mesa processed on the same wafer (2.6 mA/W at room temperature and zero bias). The increased responsivity can be explained by the quality factor of the cavity at 10  $\mu\text{m}$ ,  $Q = \tilde{\omega}_{ISB}/(\Gamma_a + \gamma_a + \gamma_{ISB}) = 10.3$ , and interpreted simply as a result of the increased light-matter interaction length induced by the cavity.

### C. Design of metamaterial Stark modulator

Our modulator is based on the linear Stark effect in a system of asymmetric tunnel-coupled quantum wells,<sup>25</sup> as presented in Fig. 3(a). The principle of operation of the device is the following. An electric field applied to the structure linearly shifts the absorption energy of the intraband transition,  $\hbar\omega_{ISB} = E_2 - E_1$ . When a laser beam impinges on the metamaterial modulator, the amplitude of the reflected signal depends on the intraband absorption at the laser frequency, which in turn depends on the applied electric field. The quantity to be maximized for the metamaterial modulator operation is the contrast between the incident and the reflected amplitude in a given voltage range. In the coupled mode theory formalism, this means maximizing the contrast  $\Delta|S_{out}/S_{in}|^2$ , or equivalently the variation of the device's total absorption,  $\Delta A_{tot}$ , for a given voltage range  $\Delta V$ .

The metamaterial modulator can be designed to operate in the three light-matter coupling regimes mentioned in Sec. II A. Pirotta *et al.* demonstrated a mid-infrared modulator that switches between

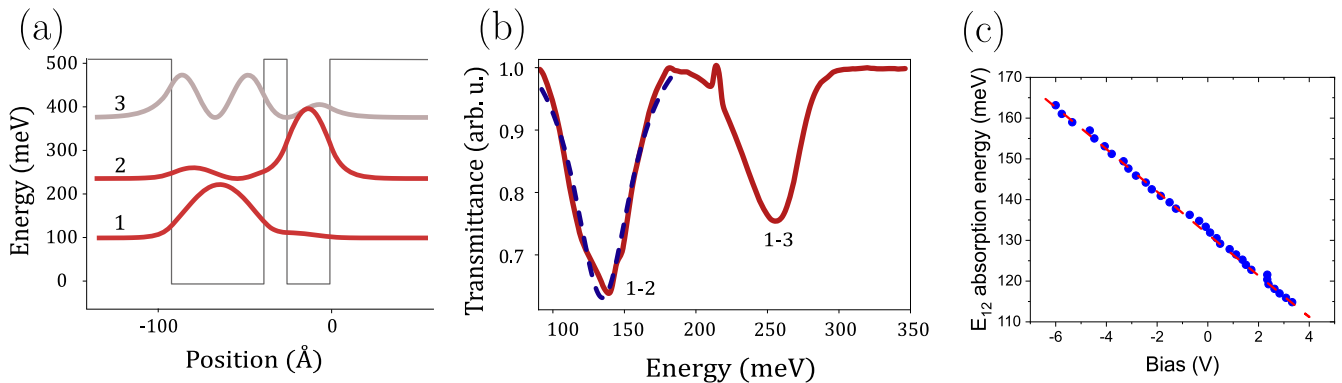


**FIG. 3.** Principle of operation of the Stark modulator. (a) Conduction band diagram of one period of the GaInAs/AlInAs Stark modulator. The square moduli of the relevant wavefunctions are plotted at the corresponding energies. The thicknesses of the wells and barriers are 5.6, 1.4, 2.6, 20 nm, where InGaAs wells are indicated in bold. (b) Transmission spectrum measured at room temperature. The two minima correspond to the transitions between the states 1-2 and 1-3. (c) Measured (blue dots) and simulated (dashed red line) energy of the transition 1-2. The Stark shift extracted from these data is 5.1 meV/V.



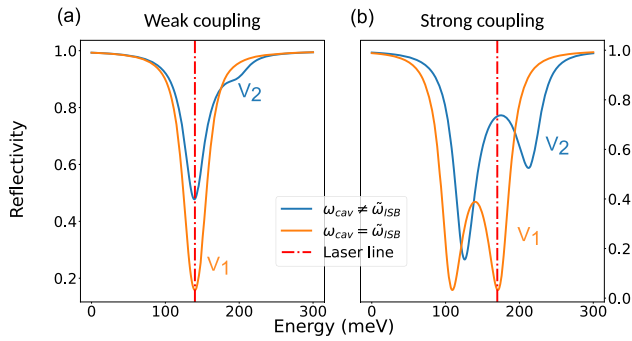


**FIG. 4.** Simulated reflectivities of two different metamaterial modulator devices with the same parameters  $\hbar\gamma_a = 2.3$  meV,  $\hbar\gamma_{ISB} = 20.1$  meV, and  $\hbar\Gamma_a \times p^2 = 151$  meV  $\mu\text{m}^2$ , as summarized in Table I. The two devices operate in different light-matter coupling regimes: their Rabi energies  $\hbar\Omega_R$  are (a) 9 meV for the one in the weak coupling regime and (b) 35 meV for the other one in the strong coupling regime. In the two panels, the intraband polarization is put in and out of resonance with the cavity by a bias voltage.

the weak and strong coupling regimes through the modulation of the electronic density in a quantum well.<sup>41</sup> In this device, the charge displacement needed for modulation has a frequency cut-off set by the electron displacement controlled by a gate voltage. This limits the bandwidth to 1 GHz. Our metamaterial modulator operates in a fundamentally different way. Light modulation is induced by a bias voltage (between  $V_1$  and  $V_2$ ) which modifies the detuning between  $\omega_{cav}$  and  $\bar{\omega}_{ISB}$ , without any charge displacement. The light-matter coupling regime corresponds to different modulator operations, as sketched in Fig. 4 and described below.

In the weak coupling regime, the losses are greater than the Rabi energy [panel 4(a)] and there is no splitting. The modulator is designed to reach the critical coupling at bias  $V_1$ , when the intraband polarization is resonant with the cavity mode. For  $\omega_{laser} = \omega_{cav}$ , the reflected intensity is negligible because of the strong metamaterial absorption. When voltage  $V_2$  is applied, the absorption at the laser frequency decreases as the intraband absorption is detuned from the cavity resonance. The reflectivity of the device is thus modulated between  $V_1$  and  $V_2$ . This effect can be enhanced by increasing the electronic density in the quantum wells. Yet, the higher electronic density also increases the coupling energy,  $\hbar\Omega_R$ , between the cavity mode and the optical resonance and therefore it brings the system into the strong coupling regime, where  $\Omega_R$  is larger than all the system's losses (cavity and intraband).

In this regime, the cavity mode of the metamaterial can be in resonance with the intraband polarization under the applied bias  $V_1$ . In this case, two absorption maxima (reflectivity minima) are observed, associated with the two polariton states. If the laser frequency is resonant with one of the polariton modes, the incident light is therefore strongly absorbed at  $V_1$ . By applying a different bias  $V_2$ , the optical transition shifts away from the resonance with the cavity mode, with a consequent change in the absorption spectrum as it is apparent in Fig. 4(b). One reflectivity minimum is preponderant, centered at a different frequency than the polariton

states at resonance. In this case, the reflected signal is maximized [panel 4(b)]. The absorption contrast  $\Delta A_{tot} = A_{tot}(V_1) - A_{tot}(V_2)$  is generally higher in the strong than in the weak coupling regime, as the polariton mode can be completely out of resonance from the laser line. This effect is expected to be even more important in the ultrastrong coupling regime as an energy gap separates the two polariton modes.<sup>51</sup>

#### D. Optimization of the metamaterial modulator geometric parameters

We describe how the metamaterial modulator concepts are applied to our Stark modulator.

The active region of our device contains 20 periods of asymmetric tunnel-coupled GaInAs/AlInAs quantum wells, lattice-matched with InP. The band diagram of one period is presented in Fig. 3(a), together with the square moduli of the relevant wavefunctions plotted at the corresponding energy. To reach the strong coupling regime, we have doped the quantum wells with a nominal value of  $6 \times 10^{18} \text{ cm}^{-3}$ , much higher than the doping level used for the QCDs.

Two transitions are optically active: from the ground to the first excited state (1–2), at  $9 \mu\text{m}$  (140 meV), and from the ground to the second excited state (1–3), at  $5 \mu\text{m}$  (260 meV), as illustrated in Fig. 3(b), presenting the room temperature transmission of the multi-quantum well system. The 1–2 resonance is quite large ( $\hbar\gamma_{ISB} = 20.1$  meV), due to interface roughness scattering and doping inhomogeneities, which can be extremely efficient for diagonal transitions.<sup>52</sup> The simulated 1–2 absorption energy as a function of the applied bias is presented in Fig. 3(c) (red line), corresponding to a Stark shift of 5.1 meV/V. This dependence was experimentally verified on a Stark modulator processed in a mesa geometry. The Stark shift was measured by using a tunable quantum cascade laser (MIRcat-QT Mid-IR Laser, DRS Daylight Solutions), operating between  $7.4$  and  $11.5 \mu\text{m}$ . The intensity transmitted through the mesa modulator was measured on a commercial mercury cadmium telluride detector. For each incident wavelength, we extract from the measurements the voltage at which the transmitted intensity is minimum. In this way, we could experimentally reconstruct the intraband absorption energy as a function of the applied bias [blue dots in Fig. 3(c)], which is in excellent agreement with the simulated one (red line).

The metamaterial modulator was fabricated in the same architecture as the metamaterial detector. Following the approach used for the metamaterial detector design, we measured the reflectivity spectra of a set of unbiased devices and fitted them within the framework of the CMT. The resulting parameters are reported in Table I. From the value of the Rabi frequency, we calculated an effective electronic density of  $2.3 \times 10^{18} \text{ cm}^{-3}$ , which is one-third of the nominal value. Coupled mode theory allowed us to simulate the metamaterial modulator operation to engineer its geometrical parameters. Figure 5(a) presents the calculated contrast  $\Delta A_{tot}$  for different  $s$  and  $p$  pairs at  $10 \mu\text{m}$  and for voltages ranging from  $V = -4$  V to  $V = 4$  V. The symbols indicate the three different operation regimes, attainable for different geometric parameters, allowed by our structure. The corresponding bias-dependent reflectivities at  $10 \mu\text{m}$  are presented in 5(b). For  $s = 1.52 \mu\text{m}$  and  $p = 3.6 \mu\text{m}$ , the

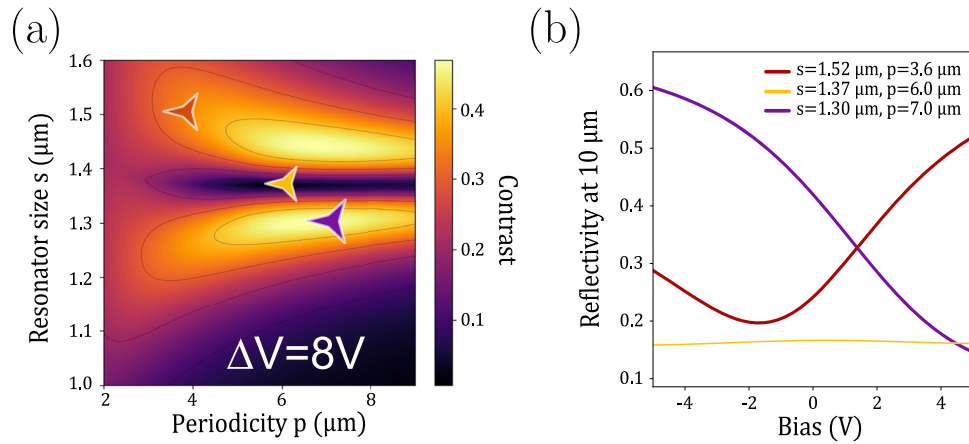


**FIG. 5.** Simulated contrast at the output of the modulator,  $\Delta|S_{out}/S_{in}|^2$ , in the bias range  $\pm 4\text{ V}$ . (a) Evolution of the contrast with the stripes' width  $s$  and spacing  $p$ . (b) Bias dependence of the reflectivity for the three sets of  $(s, p)$  parameters highlighted in panel (a).

device operates in the weak coupling regime, and the minimum reflectivity (maximum absorbance) is reached when the intraband polarization is resonant with the cavity mode. When increasing the periodicity of the metamaterial, for  $s = 1.30\text{ }\mu\text{m}$  and  $p = 7\text{ }\mu\text{m}$ , the

cavity radiative losses decrease and the device reaches the onset of the strong-coupling regime. Finally, for  $s = 1.37\text{ }\mu\text{m}$  and  $p = 6\text{ }\mu\text{m}$ , we observe a nearly null contrast when the laser and the cavity are tuned.

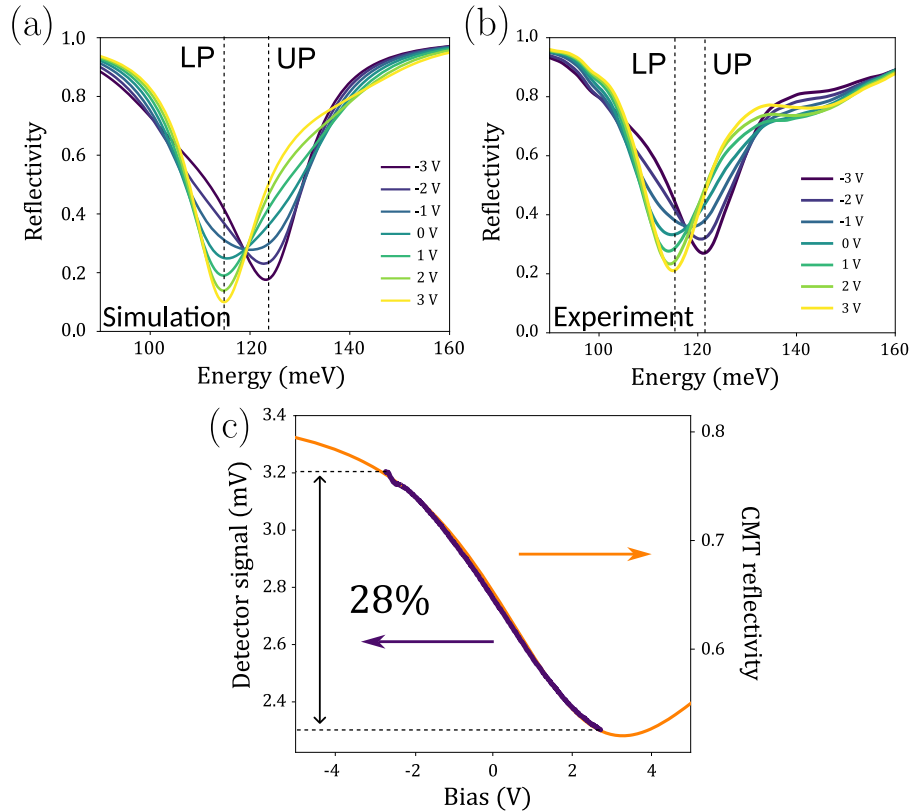


**FIG. 6.** Comparison between simulated and experimental performances of the actual modulator device at  $10\text{ }\mu\text{m}$  wavelength. (a) CMT simulations for the reflectivity spectra using the measured values presented in Table I for biases ranging from  $-3$  to  $3\text{ V}$ . (b) Measured reflectivity spectra corresponding to the simulated cases. (c) Signal acquired on the detector when changing the bias of the modulator (purple) and simulated bias-dependent reflectivity spectra (orange). The contrast of 28% obtained in the  $-2.7$  to  $2.7\text{ V}$  range is consistent with the predicted reflectivity change induced by the bias sweep.



### E. Performances of the metamaterial Stark modulator

The set of parameters chosen for fabrication was  $s = 1.27 \mu\text{m}$  and  $p = 7 \mu\text{m}$ . Figure 6(a) presents the simulated reflectivity spectra of the metamaterial modulator with these dimensions. The Stark shift results in the variation of the energy position of the reflectivity minimum with the bias. Physically, this corresponds to transferring the matter weight from the upper (UP) to the lower (LP) polariton due to the Stark shift of the intraband polarization. The contrast at a wavelength of  $10 \mu\text{m}$  between  $-3$  and  $3 \text{ V}$  is calculated to be 35%.

Figure 6(b) presents the reflectivity spectra of the metamaterial modulator measured with an FTIR using a Cassegrain microscope objective (Bruker Hyperion) for different applied bias voltages. The overall operation of the modulator corresponds very well to the predicted behavior. The extra feature observed in the experimental spectra at  $\approx 140 \text{ meV}$  is attributed to diffraction<sup>45</sup> induced by the large numerical aperture of the microscope.

Figure 6(c) presents the QCD signal when it is illuminated by a  $10 \mu\text{m}$  laser reflected by the modulator under a bias in the range between  $-2.7$  and  $2.7 \text{ V}$  (purple curve). For modulation of  $5.4 \text{ V}$  peak-to-peak, a contrast of 28% is observed, well reproduced by the CMT simulation (depicted in orange). A slightly larger modulation depth can be reached with a larger bias. However, we restricted the modulator operation to  $5.4 \text{ V}$  peak-to-peak to work close to the linear regime, which is suitable for data transmission.

When comparing the metamaterial modulator performances with those of a mesa device based on the Stark effect, as in Ref. 25, we notice several improvements introduced by the metamaterial concept. First of all, the same modulation depth can be reached with a lower applied voltage: in this work, we report a reduction by a factor of 2 with respect to Ref. 25. Second, the electrical footprint of the device is strongly reduced. Indeed, our metamaterial modulator has an electrical area of  $1.2 \times 10^3 \mu\text{m}^2$ , while the optical area is  $2.5 \times 10^3 \mu\text{m}^2$ . This reduction of the electrical area improves the

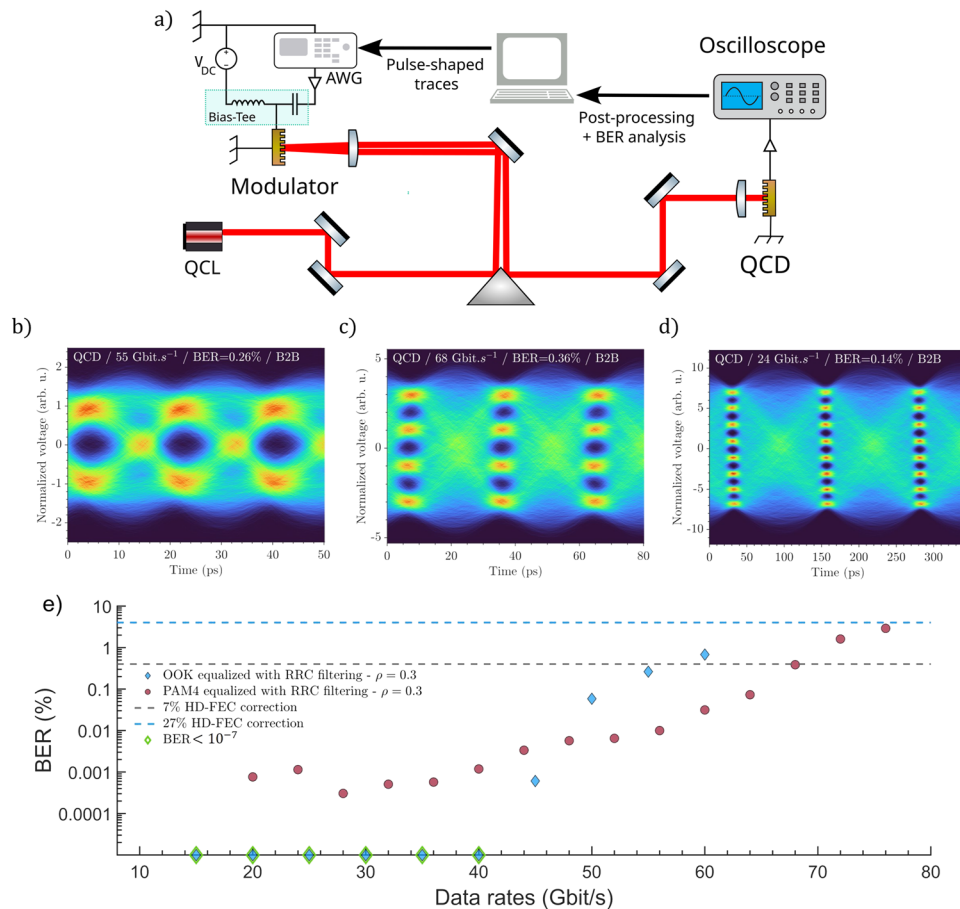


**FIG. 7.** Data transmission experiment report with (a) a sketch of the experimental setup. Eye diagrams illustrate free-space propagation (over  $\sim 2 \text{ m}$ ) for three distinct modulation formats: (b)  $55 \text{ Gbit s}^{-1}$  NRZ transmission after DFE equalization, (c)  $68 \text{ Gbit s}^{-1}$  PAM-4 transmission after DFE equalization, and (d)  $24 \text{ Gbit s}^{-1}$  PAM-8 transmission after DFE equalization. (e) Evolution of the data transmission BERs for NRZ (blue diamonds) and PAM-4 (red circles) as a function of the bitrate. The 0.4 % and 4% error thresholds are indicated with black and blue dashed lines, respectively.

frequency response of the modulator, which is flat with cutoff at 9 GHz (see [Appendix C](#)).

### III. DATA TRANSMISSION AT 10 $\mu\text{m}$ WAVELENGTH

#### A. Description of the experimental set-up

After their initial characterization, all metamaterial-based unipolar devices presented earlier are connectorized [2.92 mm connector and high-speed printed circuit board (PCB) on a copper mount] and gathered to assemble a high-speed data transmission system relying on external modulation, as presented in [Fig. 7\(a\)](#). The laser source is a room-temperature commercial quantum cascade laser (Daylight Solutions MIRcat-QT) operating at 15 °C with 100 mW output power at 10  $\mu\text{m}$  wavelength. The beam is deflected by a silver-coated prism toward a 1-inch ZnSe lens with  $F = 1$ , which focuses light on the external modulator. The insertion losses introduced by the modulator are measured to be as low as 2 dB. The reflected beam is sent back to the other face of the prism and impinges on the QCD after passing through another  $F = 1$  lens. The detector is slightly tilted (a few degrees) to avoid direct reflections into the laser cavity generating parasitic feedback effects. A 65 GSa/s arbitrary waveform generator (AWG, Keysight M8195A) is connected to the modulator through an amplifier and a bias-tee, as well as a DC power supply. The QCD is connected to a 200 GSa/s oscilloscope (Tektronix DPO70000SX) with another amplifier of 35 dB. The AWG and oscilloscope are controlled by a computer that pre-processes the traces about to be transmitted and post-processes the received data sequences. The frequency performances of the individual metamaterial devices and the full system are presented in [Appendix C](#).

#### B. Results of mid-infrared data transmission using metamaterial unipolar devices

This experiment aims to assess the viability of a data transmission link using three distinct amplitude modulation formats: 2-levels (NRZ), 4-levels (PAM-4), and 8-levels (PAM-8). Pseudo-random binary sequences (PRBS) with a length of  $2^{15}$  are generated for these formats, employing a root-raised cosine (RRC) filtering technique.<sup>53</sup> This technique facilitates the compression of the spectral footprint of the generated signal according to a compression factor  $\rho$ . After some rounds of optimization, the parameter for this filter is chosen to be  $\rho = 0.3$ . The use of  $2^{15}$ -bit long PRBS ensures a wide range of bit sequence combinations, allowing for a precise evaluation of the transmission quality. We also implement digital equalization, a critical process that substantially improves maximum data rates by addressing systematic distortions of the channel and minimizing intersymbol interference. To do so, we initially apply a fractional-spaced feed-forward equalization (FFE) scheme to the received signal with four samples per symbol, effectively equalizing the received signal.<sup>54</sup> Throughout our study, we observe substantial fluctuations in the channel leading to increased errors in the FFE equalized traces. Those fluctuations are likely to result from self-feedback induced by the reflection on the modulator, causing slow and slight intensity fluctuations. To tackle this issue, we implement a Decision-Directed Decision Feedback Equalization (DFE) technique. The high responsivity and expanded bandwidth of the devices enable higher data rates while maintaining a high

modulated output power of  $\sim 30$  mW. The quality of the transmission is assessed quantitatively through the computation of the bit error rate (BER), representing the ratio of the number of errors in the received data to the total number of bits sent. The BER is calculated over the full span of every acquired sequence, which represents  $\sim 2.5 \times 10^9$  bits at 60 Gbit  $\text{s}^{-1}$  with PAM-4 encoding. These BER values cannot exceed given levels to meet the specifications for Forward Error Correction (FEC), which is a common technique employed to correct erroneous bits.<sup>55</sup> This enables error-free transmission at the expense of a data rate reduction due to the addition of redundant bits in the data frames. We set a maximum pre-FEC BER of 0.47% corresponding to a bitrate overhead of 6.25%, which is to be associated with a hard-decision (HD) decoding to ensure error-free communication. [Figures 7\(b\)–7\(e\)](#) presents a report of the data transmission experiment with eye diagrams for the different coding schemes mentioned earlier, along with a BER graph for the two best configurations (NRZ and PAM-4). We achieved a data rate of 55 Gbit  $\text{s}^{-1}$  (51.8 Gbit  $\text{s}^{-1}$  net bitrate after redundant bit addition) NRZ while maintaining a BER of 0.26%. Similarly, we attained a data rate of 68 Gbit  $\text{s}^{-1}$  (64 Gbit  $\text{s}^{-1}$  net bitrate) PAM-4 with a BER of 0.36% [[Fig. 7\(c\)](#)]. In addition, we reached a data rate of 24 Gbit  $\text{s}^{-1}$  (22.6 Gbit  $\text{s}^{-1}$  net bitrate) PAM-8 with a BER of 0.34% [[Fig. 7\(d\)](#)]. This lower value can be attributed to an insufficient signal-to-noise ratio preventing the efficient use of a high modulation format like PAM-8. This could be compensated for with a better modulator-induced contrast and/or a higher detector responsivity.

### IV. CONCLUSION

The use of metamaterials enables a significant enhancement of the functionality of unipolar devices. Owing to their efficient electromagnetic energy confinement and the reduction of electrical area, they promote high-frequency operation devices. The understanding of the key parameters in the context of the coupled mode theory enables the design and engineering of detectors with better detectivity and retroreflector modulators with low power consumption. With these devices, we have demonstrated a single channel data transmission link, within the 8–14  $\mu\text{m}$  atmospheric transparency window, with a capacity close to 70 Gbit/s. This throughput on a single channel enabled by metamaterials is in line with modern telecommunications standards.

Remarkably, these achievements have been obtained using standard protocols for data transmission, which are well-established in the telecom industry. In other words, all the procedures to inject the rf signal into the optical carrier and out from the end-detectors rely on today's telecom technology. Our breakthrough corresponds to a new optoelectronic technology, UQO, operating on a carrier at a much greater wavelength, yet compatible with the existing protocols. Moreover, UQO relies on the same semiconductor fabrication technology and same materials as that of telecom optoelectronics. Therefore, future developments of integrated optics in the 10  $\mu\text{m}$  wavelength<sup>56,57</sup> will greatly benefit from the maturity of optoelectronic technology already developed in the near-infrared (1.55  $\mu\text{m}$ ).

A future major milestone for unipolar quantum optoelectronics is multiplexing, in terms of wavelength or phase division. Wavelength multiplexing, the ability to transmit data contemporary

on numerous channels, can be implemented in the vast bandwidth available within the unregulated 8–14  $\mu\text{m}$  transparency window by exploiting the wavelength agility characteristic of unipolar devices. At the same time, the realization of phase modulators<sup>42</sup> and stabilized<sup>58,59</sup> coherent detection would enable phase division multiplexing, which is a more efficient utilization of the system's full capacity. With these relatively straightforward adjustments, it is conceivable to achieve systems with capacity well over terabit/s.

Finally, it is important to underline that, in addition to bitrate improvements, it is necessary to demonstrate optical signal transmission over long distances, in the order of a kilometer. This is conceivable today owing to the notable enhancement in the output power of distributed feedback (DFB) quantum cascade lasers around 9  $\mu\text{m}$  that emit watt-level output power. In the near future, it is conceivable to realize a new generation of laser sources based on two-dimensional optical phased arrays or photonic crystals. These devices will enable precise active control of the beam direction toward the target and further increase the efficiency of the systems. Remarkably, sources with an active pointing arrangement hold significant appeal for mid-infrared LIDAR applications.

## ACKNOWLEDGMENTS

The authors acknowledge the financial support of the Direction Générale de l'Armement (DGA), the ENS-Thales Chair, PEPR Electronique, ANR project LIGNEDEMIR (Grant No. ANR-18CE09-0035), FETOpen 2018–2020 Horizon 2020 projects cFLOW (Grant No. 828893), and CNRS Renatech network.

## AUTHOR DECLARATIONS

### Conflict of Interest

The authors have no conflicts to disclose.

## Author Contributions

T.B. and H.D. contributed equally to this work.

**T. Bonazzi:** Conceptualization (equal); Investigation (equal); Resources (equal); Visualization (equal); Writing – review & editing (equal). **H. Dely:** Conceptualization (equal); Investigation (equal); Resources (equal); Visualization (equal); Writing – original draft (equal); Writing – review & editing (equal). **P. Didier:** Investigation (equal); Visualization (equal); Writing – original draft (equal); Writing – review & editing (equal). **D. Gacemi:** Conceptualization (equal); Investigation (equal); Resources (equal); Writing – review & editing (equal). **B. Fix:** Investigation (equal); Writing – review & editing (equal). **M. Beck:** Resources (equal); Writing – review & editing (equal). **J. Faist:** Resources (equal); Writing – review & editing (equal). **A. Harouri:** Resources (equal). **I. Sagnes:** Investigation (equal); Resources (equal); Writing – review & editing (equal). **F. Grillot:** Supervision (equal); Validation (equal); Writing – review & editing (equal). **A. Vasanelli:** Conceptualization (equal); Supervision (equal); Validation (equal); Writing – original draft (equal); Writing – review & editing (equal). **C. Sirtori:** Conceptualization (lead); Supervision (equal); Validation (lead); Writing – original draft (equal); Writing – review & editing (equal).

## DATA AVAILABILITY

Data underlying the results presented in this paper are not publicly available at this time but may be obtained from the corresponding author upon reasonable request.

## APPENDIX A: EQUIVALENCE BETWEEN $\Delta A_{tot}$ AND THE CONTRAST INDUCED BY THE MODULATOR

In this appendix, we briefly demonstrate that we can optimize the power dissipation of the modulator or its contrast equally. Under a monochromatic excitation  $S_{in} = s_0 e^{j\omega t}$  as described in Sec. II A, the excitation in the active region  $P$  can be expressed from Eq. (2) as

$$P = \frac{i\Omega_R}{i(\omega - \tilde{\omega}_{ISB}) + \gamma_{ISB}} a,$$

which leads, according to Eq. (2), to a normalized total dissipated power:

$$A_{tot} = 2 \left( \gamma_a + \frac{\gamma_{ISB} \Omega_R^2}{(\omega - \tilde{\omega}_{ISB})^2 + \gamma_{ISB}^2} \right) \left| \frac{a}{S_{in}} \right|^2.$$

The power reflected by the modulator is

$$\left| \frac{S_{out}}{S_{in}} \right|^2 = 1 + 2\Gamma_a \left| \frac{a}{S_{in}} \right|^2 - 2\sqrt{2\Gamma_a} \operatorname{Re} \frac{a}{S_{in}}.$$

After some algebra, the real part of  $a/S_{in}$  is shown to be

$$\operatorname{Re} \left( \frac{a}{S_{in}} \right) = \frac{1}{\sqrt{2\Gamma_a}} \left( (\gamma_a + \Gamma_a) + \frac{\gamma_{ISB} \Omega_R^2}{(\omega - \tilde{\omega}_{ISB})^2 + \gamma_{ISB}^2} \right) \left| \frac{a}{S_{in}} \right|.$$

Reporting the last expression into the one of  $A_{tot}$  yields the final result as the energy conservation equation,

$$\left| \frac{S_{out}}{S_{in}} \right|^2 + A_{tot} = 1.$$

Thus, optimizing the contrast  $\Delta \left| \frac{S_{out}}{S_{in}} \right|^2$  is equivalent to optimizing the power dissipation of the modulator  $\Delta A_{tot}$ .

## APPENDIX B: ANTENNA RESONATOR FABRICATION

The fabrication process for both the modulator and detector resonators is identical and is presented below. The heterostructure is metallized with Ti/Au (15/300 nm) and wafer-bonded through the thermocompression of a bulk GaAs wafer with an identical metallization. The original InP substrate is selectively removed using HCl. Ti/Au/Ni 60  $\mu\text{m} \times 60 \mu\text{m}$  resonators are patterned on the active region using e-beam lithography and then etched using a Cl-based Inductively Coupled Plasma (ICP) method down to the ground gold layer. A 150  $\mu\text{m} \times 300 \mu\text{m}$  protective resist layer is applied around the resonators before etching the bottom gold in a KI/I<sub>2</sub> solution. The Ti at the bottom of the wafer-bonding layer acts as an etch-stop and is then removed by RIE. Following the deposition of a sacrificial support of reflowed S1818 resist for the air bridge, the Ti/Au 50  $\Omega$  coplanar waveguide is evaporated in one step using negative resist AZ5214 E for patterning. A photoresist stripper (SVC 14) is preferred over the standard acetone lift-off method to ensure the bridge is properly freed from the resist.

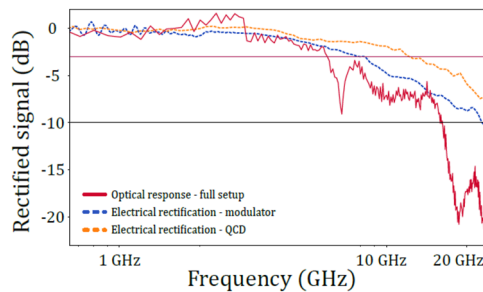


**FIG. 8.** Frequency characterization of the modulator (blue curve) and the detector (orange curve) obtained using electrical rectification. The bandwidth of the full system is also assessed (red curve) using an optical carrier as in the actual data transmission experiment.

## APPENDIX C: FREQUENCY CHARACTERISATION OF THE METAMATERIAL DEVICES

Figure 8 presents the electrical bandwidth of both the modulator and detector measured using an electrical rectification technique, as well as the electrical bandwidth of the whole data transmission system acquired in operational conditions using an actual mid-infrared carrier. Both devices' frequency responses are flat, with cutoffs at 9 GHz for the modulator and 12 GHz for the detector. The full system exhibits a sharp dip around 8 GHz before a small plateau and finally a dramatic decrease of the response starting from 16 GHz. This is due to an impedance mismatch between the device and the connector inducing parasitic radiation from the injected microwave power.<sup>29</sup>

## REFERENCES

- <sup>1</sup>A. Trichili, M. A. Cox, B. S. Ooi, and M.-S. Alouini, *J. Opt. Soc. Am. B* **37**, A184 (2020).
- <sup>2</sup>Y. Horst, B. I. Bitachon, L. Kulmer, J. Brun, T. Blatter, J.-M. Conan, A. Montmerle-Bonnefois, J. Montri, B. Sorrente, C. B. Lim *et al.*, *Light: Sci. Appl.* **12**, 153 (2023).
- <sup>3</sup>P. Corrigan, R. Martini, E. A. Whittaker, and C. Bethea, *Opt. Express* **17**, 4355 (2009).
- <sup>4</sup>J. J. Liu, B. L. Stann, K. K. Klett, P. S. Cho, and P. M. Pellegrino, *Proc. SPIE* **11133**, 1113302 (2019).
- <sup>5</sup>M. A. Esmail, A. Ragheb, H. Fathallah, and M. S. Alouini, *IEEE Photonics J.* **9**, 1 (2017).
- <sup>6</sup>L. Wang, T. Xing, S. Hu, X. Wu, H. Wu, J. Wang, and H. Jiang, *Opt. Express* **25**, 3373 (2017).
- <sup>7</sup>B. Cole, L. Goldberg, S. Chinn, L. A. Pomeranz, K. T. Zawilski, P. G. Schunemann, and J. McCarthy, *Opt. Lett.* **43**, 1099 (2018).
- <sup>8</sup>C. R. Petersen, U. Möller, I. Kubat, B. Zhou, S. Dupont, J. Ramsay, T. Benson, S. Sujecki, N. Abdel-Moneim, Z. Tang *et al.*, *Nat. Photonics* **8**, 830 (2014).
- <sup>9</sup>M. Montesinos-Ballester, C. Lafforgue, J. Frigerio, A. Ballabio, V. Vakarin, Q. Liu, J. M. Ramirez, X. Le Roux, D. Bouville, A. Barzaghi *et al.*, *ACS Photonics* **7**, 3423 (2020).
- <sup>10</sup>J. Faist, F. Capasso, D. L. Sivco, C. Sirtori, A. L. Hutchinson, and A. Y. Cho, *Science* **264**, 553 (1994).
- <sup>11</sup>J. Haas and B. Mizaikoff, "Advances in mid-infrared spectroscopy for chemical analysis," *Annu. Rev. Anal. Chem.* **9**, 45 (2016).

- <sup>12</sup>L. Zhang, G. Tian, J. Li, and B. Yu, *Appl. Spectrosc.* **68**, 1095 (2014).
- <sup>13</sup>B. Jean and T. Bende, "Mid-IR laser applications in medicine," in *Solid-State Mid-Infrared Laser Sources*, edited by I. T. Sorokina and K. L. Vodopyanov (Springer, Berlin, Heidelberg, 2003), pp. 530–565.
- <sup>14</sup>F. K. Tittel and F. K. Tittel, *Opt. Eng.* **49**, 111123 (2010).
- <sup>15</sup>R. Martini *et al.*, *Elec. Lett.* **37**, 191 (2001).
- <sup>16</sup>S. Blaser, *Elec. Lett.* **37**, 778 (2001).
- <sup>17</sup>R. Martini, *Elec. Lett.* **38**, 181 (2002).
- <sup>18</sup>H. Dely, *Nature Commun.* **15**, 8040 (2024).
- <sup>19</sup>K. Zou, K. Pang, H. Song, J. Fan, Z. Zhao, H. Song, R. Zhang, H. Zhou, A. Minoofar, C. Liu *et al.*, *Nat. Commun.* **13**, 7662 (2022).
- <sup>20</sup>R. Ferreira and G. Bastard, *Phys. Rev. B* **40**, 1074 (1989).
- <sup>21</sup>B. Meng and Q. J. Wang, *Opt. Express* **20**, 1450 (2012).
- <sup>22</sup>P. Grant, R. Dudek, M. Buchanan, and H. Liu, *IEEE Photonics Technol. Lett.* **18**, 2218 (2006).
- <sup>23</sup>M. Saemian, L. D. Balzo, D. Gacemi, Y. Todorov, E. Rodriguez, O. Lopez, B. Darquie, L. Li, A. G. Davies, E. Linfield, A. Vasanelli, and C. Sirtori, *Nanophotonics* **13**, 1765 (2024).
- <sup>24</sup>B. Levine, *J. Appl. Phys.* **74**, R1 (1993).
- <sup>25</sup>H. Dely, T. Bonazzi, O. Spitz, E. Rodriguez, D. Gacemi, Y. Todorov, K. Pantzas, G. Beaudoin, I. Sagnes, L. Li, A. G. Davies, E. H. Linfield, F. Grillot, A. Vasanelli, and C. Sirtori, *Laser Photonics Rev.* **16**, 2100414 (2022).
- <sup>26</sup>Y. Yao, A. Hoffman, and C. Gmachl, *Nat. Photonics* **6**, 432 (2012).
- <sup>27</sup>L. Gendron, M. Carras, A. Huynh, V. Ortiz, C. Koeniguer, and V. Berger, *Appl. Phys. Lett.* **85**, 2824 (2004).
- <sup>28</sup>C. Sirtori, F. Capasso, D. L. Sivco, A. L. Hutchinson, and A. Y. Cho, *Appl. Phys. Lett.* **60**, 151 (1992).
- <sup>29</sup>P. Didier, H. Dely, T. Bonazzi, O. Spitz, E. Awwad, É. Rodriguez, A. Vasanelli, C. Sirtori, F. Grillot *et al.*, *Adv. Photonics* **4**, 056004 (2022).
- <sup>30</sup>C. Walther, G. Scalari, M. I. Amanti, M. Beck, and J. Faist, *Science* **327**, 1495 (2010).
- <sup>31</sup>L. Xu, D. Chen, C. A. Curwen, M. Memarian, J. L. Reno, T. Itoh, and B. S. Williams, *Optica* **4**, 468 (2017).
- <sup>32</sup>J. Pérez-Urquiza, Y. Todorov, L. Li, A. G. Davies, E. H. Linfield, C. Sirtori, J. Madéo, and K. M. Dani, *ACS Photonics* **8**, 412 (2021).
- <sup>33</sup>D. Palaferri, Y. Todorov, A. Bigioli, A. Mottaghizadeh, D. Gacemi, A. Calabrese, A. Vasanelli, L. Li, A. G. Davies, E. H. Linfield *et al.*, *Nature* **556**, 85 (2018).
- <sup>34</sup>A. Benz, M. Krall, S. Schwarz, D. Dietze, H. Detz, A. M. Andrews, W. Schrenk, G. Strasser, and K. Unterrainer, *Sci. Rep.* **4**, 4269 (2014).
- <sup>35</sup>G. Quinchard, C. Mismar, M. Hakl, J. Pereira, Q. Lin, S. Lepillet, V. Trinité, A. Evrigen, E. Peytavit, J. Reverchon *et al.*, *Appl. Phys. Lett.* **120**, 091108 (2022).
- <sup>36</sup>H. T. Miyazaki, T. Mano, T. Kasaya, H. Osato, K. Watanabe, Y. Sugimoto, T. Kawazu, Y. Arai, A. Shigetou, T. Ochiai, Y. Jimba, and H. Miyazaki, *Nat. Commun.* **11**, 565 (2020).
- <sup>37</sup>M. F. Hainey, T. Mano, T. Kasaya, T. Ochiai, H. Osato, K. Watanabe, Y. Sugimoto, T. Kawazu, Y. Arai, A. Shigetou, and H. T. Miyazaki, *Nanophotonics* **9**, 3373 (2020).
- <sup>38</sup>M. Hakl, Q. Lin, S. Lepillet, M. Billet, J.-F. Lampin, S. Pirotta, R. Colombelli, W. Wan, J. Cao, H. Li *et al.*, *ACS Photonics* **8**, 464 (2021).
- <sup>39</sup>Q. Lin, M. Hakl, S. Lepillet, H. Li, J.-F. Lampin, E. Peytavit, and S. Barbieri, *Optica* **10**, 1700 (2023).
- <sup>40</sup>J. Lee, S. Jung, P.-Y. Chen, F. Lu, F. Demmerle, G. Boehm, M.-C. Amann, A. Alù, and M. A. Belkin, *Adv. Opt. Mater.* **2**, 1057 (2014).
- <sup>41</sup>S. Pirotta, N.-L. Tran, A. Jollivet, G. Biasiol, P. Crozat, J.-M. Manceau, A. Bousseksou, and R. Colombelli, *Nat. Commun.* **12**, 799 (2021).
- <sup>42</sup>H. Chung, I. Hwang, J. Yu, G. Boehm, M. A. Belkin, and J. Lee, *Adv. Sci.* **10**, 2207520 (2023).
- <sup>43</sup>Y. Todorov, L. Tosetto, J. Teissier, A. M. Andrews, P. Klang, R. Colombelli, I. Sagnes, G. Strasser, and C. Sirtori, *Opt. Express* **18**, 13886 (2010).
- <sup>44</sup>S. Fan, W. Suh, and J. D. Joannopoulos, *J. Opt. Soc. Am. A* **20**, 569 (2003).

- <sup>45</sup>E. Rodriguez, T. Bonazzi, H. Dely, M. Mastrangelo, K. Pantzas, G. Beaudoin, I. Sagnes, A. Vasanelli, Y. Todorov, and C. Sirtori, *Opt. Express* **30**, 20515 (2022).
- <sup>46</sup>M. Helm, *Chapter 1 the Basic Physics of Intersubband Transitions, Semiconductors and Semimetals Vol. 62* (Elsevier, 1999), pp. 1–99.
- <sup>47</sup>Y. Todorov, A. M. Andrews, R. Colombelli, S. De Liberato, C. Ciuti, P. Klang, G. Strasser, and C. Sirtori, *Phys. Rev. Lett.* **105**, 196402 (2010).
- <sup>48</sup>C. Ciuti, G. Bastard, and I. Carusotto, *Phys. Rev. B* **72**, 115303 (2005).
- <sup>49</sup>P. Reininger, B. Schwarz, H. Detz, D. MacFarland, T. Zederbauer, A. M. Andrews, W. Schrenk, O. Baumgartner, H. Kosina, and G. Strasser, *Appl. Phys. Lett.* **105**, 091108 (2014).
- <sup>50</sup>L. Sapienza, A. Vasanelli, C. Ciuti, C. Manquest, C. Sirtori, R. Colombelli, and U. Gennser, *Appl. Phys. Lett.* **90**, 201101 (2007).
- <sup>51</sup>B. Askenazi, A. Vasanelli, A. Delteil, Y. Todorov, L. C. Andreani, G. Beaudoin, I. Sagnes, and C. Sirtori, *New J. Phys.* **16**, 043029 (2014).
- <sup>52</sup>E. Benveniste, A. Vasanelli, A. Delteil, J. Devenson, R. Teissier, A. Baranov, A. M. Andrews, G. Strasser, I. Sagnes, and C. Sirtori, *Appl. Phys. Lett.* **93**, 131108 (2008).
- <sup>53</sup>J. G. Proakis, *Digital Communications* (McGraw-Hill, Higher Education, 2008).
- <sup>54</sup>J. G. Proakis and M. Salehi, *Digital Communications* (McGraw-Hill, New York, 2001), Vol. 4.
- <sup>55</sup>L. M. Zhang and F. R. Kschischang, *J. Lightwave Technol.* **32**, 1999 (2014).
- <sup>56</sup>S. Jung, D. Palaferri, K. Zhang, F. Xie, Y. Okuno, C. Pinzone, K. Lascola, and M. A. Belkin, *Optica* **6**, 1023 (2019).
- <sup>57</sup>K. Zhang, G. Böhm, and M. A. Belkin, *Appl. Phys. Lett.* **120**, 061106 (2022).
- <sup>58</sup>B. Argence, B. Chanteau, O. Lopez, D. Nicolodi, M. Abgrall, C. Chardonnet, C. Daussy, B. Darquié, Y. Le Coq, and A. Amy-Klein, *Nat. Photonics* **9**, 456 (2015).
- <sup>59</sup>B. Chomet, D. Gacemi, O. Lopez, L. Del Balzo, A. Vasanelli, Y. Todorov, B. Darquié, and C. Sirtori, *Appl. Phys. Lett.* **122**, 231102 (2023).